PROCEEDINGS A

royalsocietypublishing.org/journal/rspa

Research

Article submitted to journal

Subject Areas:
biomathematics, applied mathematics, mathematical modelling

Keywords:
Wilson-Cowan, delay-coupled masses, ring network, bifurcation, chaos

Author for correspondence:
Jonathan J Crofts
e-mail: jonathan.crofts@ntu.ac.uk

THE ROYAL SOCIETY PUBLISHING

Bifurcations and synchrony in a ring of delayed Wilson-Cowan oscillators

I. Pinder, M. R. Nelson and J. J. Crofts

School of Science and Technology, Department of Physics and Mathematics, Nottingham Trent University, Nottingham, NG11 8NS, UK

Ring structures are crucial in network neuroscience, enabling the integration of neural information through closed loop circuits within feedback systems. Here, we use numerical bifurcation analysis to explore time delay effects on a ring of delay-coupled Wilson-Cowan masses. Investigating a low-dimensional 'self-coupled' version of the aforementioned system, we uncover the bifurcation structure of the synchronisation manifold, and unveil a diverse array of dynamic synchronisation patterns that emerge as a consequence of Hopf branch crossings and subsequent higher-order bifurcations. Analysis of the full system reveals transverse instabilities in the synchronised state for large regions of parameter space, with the ring network architecture promoting various dynamics depending on the balance between coupling strength and delay time. Under weak coupling, emergent oscillations are generally synchronous or anti-phase synchronous, with transitions between them triggered by a torus bifurcation of a periodic orbit. Regions of synchronous and anti-phase synchronous solutions are delineated by weakly chaotic borders due to the breakdown of the torus. As coupling strength increases, the bifurcation diagram displays more overlapped branching structure, resulting in increasingly complicated, multistable dynamics.

1. Introduction

Networks of coupled oscillators play a significant role in the modelling of a wide range of processes in neuroscience, such as neural activity synchronisation and desynchronisation [1], and the formation of complex patterns of activity in the brain such as those observed via contemporary noninvasive technologies [2]. Finite transmission speeds of information flow within the brain

motivate considerable interest in understanding network models with space-dependent time delays [3,4]. Recent work in this area has shown that incorporating time delays in the coupling terms can result in the formation of novel dynamic behaviours such as travelling waves [5], chimera states [6,7], and frequency-locking [8,9], the understanding of which can provide insights into the mechanisms underlying different neural phenomena in health and disease. We recommend the paper by Campbell [10] for a recent review of time delays specific to neural systems.

This paper is devoted to the study of a bidirectionally coupled ring of neural oscillators, with each node representing a functional unit that can be described by a neural mass model (NMM) [11]. More specifically, neural activity is described using the Wilson-Cowan model, which is a simple model for describing the activity of large populations of neurons [12]. The model incorporates two equations for each mass: one for excitatory neurons and one for inhibitory neurons, as well as two time delays: one within (or intra) population and one between (or inter) populations. It is worth noting that, although the classic single node Wilson-Cowan model has been widely investigated [13], including expansions to networked models [14–18], the delayed system is substantially less well studied. Coombes and Lang [19] investigated a delayed version of the single node Wilson-Cowan model in which they deployed a combined analytic/computational approach to investigate the contribution of intra-population delays to the generation of rhythmic neural activity patterns. More recently, Conti and Van Gorder [20] extended this model to networks and performed a numerical exploration of the impact of network heterogeneity on the resilience of observed neural dynamics using a range of toy networks including a ring, path, lattice and complete network.

The present study deploys a combined computational and mathematical approach, which significantly extends the related work by the authors in [20] to reveal the impact of inter-nodal time delays (between 'brain regions') on the onset of oscillations and synchrony in a ring network of neural masses. To investigate the synchrony properties of our model, we introduce a low-dimensional system known as the self-coupled model [21–23] that describes the dynamics of our NMM restricted to the synchronisation manifold. Unlike classical synchronisation studies that usually focus on diffusive coupling or its variations [24], the synchronous solutions of our NMM do not align with the uncoupled system; instead, they remain dependent on both the coupling strength and inter-nodal delay in a nontrivial manner. Thus, studying the reduced model enables us to reveal how important system parameters influence the onset of synchronised oscillatory states. Next we consider the extent to which the ring network architecture impacts the stability properties of the aforementioned synchronous solutions by studying a ring of 6 neural masses. Numerical simulations reveal a wide range of dynamics, such as mixed-mode oscillations and chaos, as long as the coupling strength is not excessively high, in which case the dynamics are quiescent and independent of the delay parameter. Crucially, there exist large regions of parameter space in which the network dynamics become increasingly sensitive to transverse instabilities in the synchronisation manifold, which can switch abruptly between on and off states, giving rise to complex multistable spatiotemporal dynamics.

The structure of the paper is as follows. In §2 we describe the network model deployed for simulating and analysing admissible network activity patterns on a ring architecture. In §3 our analysis focuses on the synchronisation manifold, where we examine the bifurcation structure of synchronised solutions in our delay-coupled network model. We start with a linear stability analysis of the equilibrium solution and show that this solution destabilises either through a sub- or super-critical Andronov-Hopf bifurcation, depending on the value of the inter-nodal delay. Under further parameter variations, we observe a variety of synchronised dynamics including quasiperiodicity and chaos, which arise from higher-order bifurcations that manifest due to branch crossings. Section 4 is devoted to similar questions in a ring of coupled masses. Our analysis indicates that in the networked system, low-level coupling generally leads to the separation of solutions by weakly chaotic regions into two distinct types: synchronised and anti-phase synchronised solutions. Crucially, the stability properties of the synchronisation manifold,

which are determined by the underlying network structure, dictate which of the different types of solutions the system converges to. For larger values of coupling the network dynamics become increasingly sensitive due to transverse instabilities in the synchronisation manifold leading to complicated multistable dynamics. We conclude in §5 by giving a brief overview of our results and discussing avenues of future research.

2. The model

In this work we deploy the population model due to Wilson and Cowan [12]. The model considers two populations of excitatory and inhibitory neurons and neural activity is described by the following system

$$\begin{aligned}\frac{\mathrm{d}u_i}{\mathrm{d}t} &= -u_i(t) + f(c_1 u_i(t-\tau) + c_2 v_i(t-\tau) + P + \epsilon \sum_j w_{ij} u_i(t-\rho)),\\ \frac{\mathrm{d}v_i}{\mathrm{d}t} &= -v_i(t) + f(c_3 u_i(t-\tau) + c_4 v_i(t-\tau) + Q),\end{aligned} \tag{2.1}$$

for $i = 1, 2, \ldots, n$. Here, u_i and v_i represent the synaptic activity of the two populations, f denotes a firing rate function given by

$$f(x) = \frac{1}{1 + e^{-\beta x}}, \tag{2.2}$$

and ϵ is the coupling strength. The parameters c_1, c_2, c_3 and c_4 denote the strength of interaction between sub-populations within a node, whilst P and Q are control parameters representing basal inputs to each node. In our experiments we chose $\beta = 60, P = 0.65, Q = 0.5, c_1 = c_3 = -1,\ c_2 = -0.4$ and $c_4 = 0$ in agreement with [19]. We note that some other authors [8,20] incorporate a time scaling parameter in front of each derivative in (2.1), which allows the model to be tuned to recover biological rhythms with realistic frequencies. Here, following [19], we set both of these time scalings to unity, and present our analysis in terms of nondimensionalised time units that absorb these natural frequencies.

The matrix $W \in \mathrm{R}^{n\times n}$ is the scaled adjacency matrix given by

$$W = D^{-1}A, \tag{2.3}$$

where $A_{ij} = 1$ if nodes i and j are connected and zero otherwise. D is the diagonal matrix of degrees, *i.e.*

$$D = \begin{pmatrix} k_1 & & \\ & \ddots & \\ & & k_n \end{pmatrix}. \tag{2.4}$$

Here, k_i denotes the node degree which counts the neighbours of node i. It follows that the row-sum of the weight matrix W is constant:

$$\sum_{j=1}^{n} w_{ij} = 1, \tag{2.5}$$

a condition that ensures the existence of a fully synchronised solution to (2.1). For a detailed description of the conditions under which synchronous solutions exist in populations of locally interacting elements, see the review by Arenas *et al.* [24]. For more specific information related to our studies, see the more recent papers by Campbell *et al.* [21,22].

The model incorporates two delays: an intra-node delay, τ, which describes transmission of information within each neural population; and an inter-node delay, ρ, which represents the time taken for a signal to propagate between distant brain regions. In our experiments, the intra-node delay was held constant at $\tau = 0.5$ whilst the inter-node delay, ρ, acts as a bifurcation parameter with which to explore the role of delays on the dynamics of the coupled system in (2.1). For $\epsilon = 0$, each of the decoupled units behaves as in [19], displaying a range of behaviours

including quiescent, periodic and chaotic motion. For our chosen parameter values, decoupling (2.1) reduces the network dynamics to a set of identical self-sustained oscillators [19,25] and so by continuity, we expect that for small ϵ and ρ the full system in (2.1) behaves accordingly. In what follows, we consider the extent to which the dynamics of (2.1) are impacted as the coupling strength, ϵ, and inter-nodal delay, ρ, are systematically varied.

3. Dynamics on the synchronisation manifold

The model (2.1) alongside the constraints in (2.5) admits synchronous solutions $(u_i(t), v_i(t)) = (u_s(t), v_s(t))$, for $i = 1, \ldots, n$, such that the functions (u_s, v_s) satisfy the equation

$$\begin{aligned} \frac{\mathrm{d}u}{\mathrm{d}t} &= -u(t) + f(c_1 u(t-\tau) + c_2 v(t-\tau) + \epsilon u(t-\rho) + P), \\ \frac{\mathrm{d}v}{\mathrm{d}t} &= -v(t) + f(c_3 u(t-\tau) + c_4 v(t-\tau) + Q). \end{aligned} \tag{3.1}$$

In the above, we have omitted the subscript s for brevity. Importantly, this equation is independent of the network structure owing to the constraint given in Equation (2.5), and as a consequence, synchronous solutions of the networked system in (2.1) can be described by analysing the simpler self-coupled DDE model in (3.1).

Importantly, by studying the self-coupled DDE model above, we are restricting ourselves to the synchronisation manifold defined by $\mathcal{M} = \{(u_1, v_1) = (u_2, v_2) = \cdots = (u_n, v_n)\}$. Thus, the manifestation of the dynamics discussed in this section will depend on the stability of the synchronisation manifold $\mathcal{M}$, which is contingent on the specific network under consideration. In §4, we will examine the impact of network properties on the stability of the synchronization manifold, specifically when exploring admissible network states for a ring network.

(a) Linear stability analysis of fixed point

From the above, it follows that the unique equilibrium solution of (2.1), which we denote by (u^*, v^*), can be determined by solving the equations

$$P = f^{-1}(u^*) - (c_1 + \epsilon)u^* - c_2 v^* \quad \text{and} \quad Q = f^{-1}(v^*) - c_3 u^* - c_4 v^*, \tag{3.2}$$

which are derived by setting the right-hand sides of (3.1) to zero. Here, $f^{-1}(z) = \beta^{-1} \ln(z/(1-z))$.

To study the bifurcation structure and stability of synchronous solutions of (2.1) we compute eigenvalues as solutions of the characteristic equation

$$\Delta(\lambda) = \det\left[\lambda I - A - Be^{-\lambda\tau} - Ce^{-\lambda\rho}\right] = 0, \tag{3.3}$$

where I is the 2×2 identity matrix and the matrices A, B and C are given by

$$A = (\partial \mathbf{F}/\partial \mathbf{x}(t))(x^*), \quad B = (\partial \mathbf{F}/\partial \mathbf{x}(t-\tau))(x^*) \quad \text{and} \quad C = (\partial \mathbf{F}/\partial \mathbf{x}(t-\rho))(x^*),$$

with $\mathbf{x}^* = \begin{pmatrix} u^*, & v^* \end{pmatrix}$ and the function $\mathbf{F}(\mathbf{x}(t), \mathbf{x}(t-\tau), \mathbf{x}(t-\rho))$ representing the right-hand side of the differential equations in (3.1). More specifically, we have that

$$A = \begin{pmatrix} -1 & 0 \\ 0 & -1 \end{pmatrix}, \quad B = \begin{pmatrix} c_1\beta u^*(1-u^*) & c_2\beta u^*(1-u^*) \\ c_3\beta v^*(1-v^*) & c_4\beta v^*(1-v^*) \end{pmatrix}, \quad C = \begin{pmatrix} \epsilon\beta u^*(1-u^*) & 0 \\ 0 & 0 \end{pmatrix}, \tag{3.4}$$

and so the characteristic equation reads

$$\Delta(\lambda) = \det \begin{pmatrix} \lambda + 1 - \beta u^*(1-u^*)(c_1 e^{-\lambda\tau} + \epsilon e^{-\lambda\rho}) & -c_2\beta u^*(1-u^*)e^{-\lambda\tau} \\ -c_3\beta v^*(1-v^*)e^{-\lambda\tau} & \lambda + 1 - c_4\beta v^*(1-v^*)e^{-\lambda\tau} \end{pmatrix}. \tag{3.5}$$

Substituting $\lambda = i\omega$ in the above and separating real and imaginary parts give the following conditions for a Hopf bifurcation:

$$\begin{aligned} 0 = &(1 - k_1\cos(\omega\tau) - k_2\cos(\omega\rho))(1 - k_3\cos(\omega\tau)) \\ &- (\omega + k_1\sin(\omega\tau) + k_2\sin(\omega\rho))(\omega + k_3\sin(\omega\tau)) \\ &- k_4\cos(2\omega\tau) \end{aligned} \tag{3.6}$$

and

$$\begin{aligned} 0 = &(1 - k_1\cos(\omega\tau) - k_2\cos(\omega\rho))(\omega + k_3\sin(\omega\tau)) \\ &+ (\omega + k_1\sin(\omega\tau) + k_2\sin(\omega\rho))(1 - k_3\cos(\omega\tau)) \\ &+ k_4\sin(2\omega\tau). \end{aligned} \tag{3.7}$$

Here,

$$k_1 = c_1\beta u^*(1-u^*), \quad k_2 = \epsilon\beta u^*(1-u^*), \quad k_3 = c_4\beta v^*(1-v^*)$$

and

$$k_4 = c_2c_3\beta^2 u^*(1-u^*)v^*(1-v^*).$$

Simultaneous solution of equations (3.6) and (3.7) define a Hopf bifurcation and the birth of synchronous periodic solutions of (2.1).

(b) Numerical bifurcation analysis

In this section we investigate the synchronised solutions of (2.1) by studying (3.1) using numerical simulation and numerical bifurcation analysis. We deploy the software package DDE-BIFTOOL [26] to detect and follow bifurcations of the fixed points discussed in the previous section and to follow branches of stable and unstable periodic orbits under variation of the parameters controlling inter-nodal delay, ρ, and coupling strength, ϵ. In the current context, it should be emphasized that the term 'stability' (or 'instability') pertains to the stability within the synchronization manifold, rather than the global stability of a synchronized solution in the full system defined by (2.1), which relies on the specific network being investigated.

Figure 1(a) shows a curve of Andronov-Hopf (AH) bifurcations of fixed points in the (ρ, ϵ) parameter plane corresponding to solutions of (3.6, 3.7). Solid lines correspond to supercritical AH bifurcations and dashed lines subcritical AH bifurcations, with changes in criticality separated by Bautin bifurcations, which are labelled with red circles. The AH branch is confined to the strip of parameter space for which $\epsilon \in [0.3125, 0.3705]$ and possesses a 'periodic-like' looping structure that causes the curve to self-intersect resulting in double Hopf bifurcations, which we label with black diamonds. The repetitive nature of the AH branch is well documented for delay differential equations (see, for example, [27,28]) and is due to the existence of higher-order harmonics in the delay variable. For large values of coupling (*i.e.* values below the AH bifurcation curve in Figure 1(a)) the steady state is stable, with all eigenvalues having negative real parts, independent of the inter-nodal delay, ρ; however, once destabilised by the AH bifurcation, the steady state remains unstable and periodic solutions persist.

Figures 1(b) and 1(c) show bifurcation sets emanating from the Bautin bifurcations and double Hopf bifurcation observed on the first two looping structures in Figure 1(a), respectively. These additional bifurcation curves describe stability loss for periodic orbits born from the AH bifurcations in 1(a) and can be classified according to their Floquet multipliers: TB stands for torus bifurcation, which results when a periodic orbit loses stability via a pair of complex conjugate Floquet multipliers, $\mu_{1,2} = e^{\pm i\theta}$, crossing the unit circle, thus resulting in the birth of an invariant torus; SNPO stands for saddle node of periodic orbits, which results in the birth or death of a pair of periodic orbits as a single Floquet multiplier leaves the unit circle through $\mu = 1$; and PD stands for period doubling bifurcation which describes the situation in which a periodic orbit splits into two orbits, one of which has twice the period of the original one, which loses stability as the multiplier leaves the unit circle through $\mu = -1$. (See Seydel's text [29] for an excellent and detailed discussion of this topic, along with further references.)

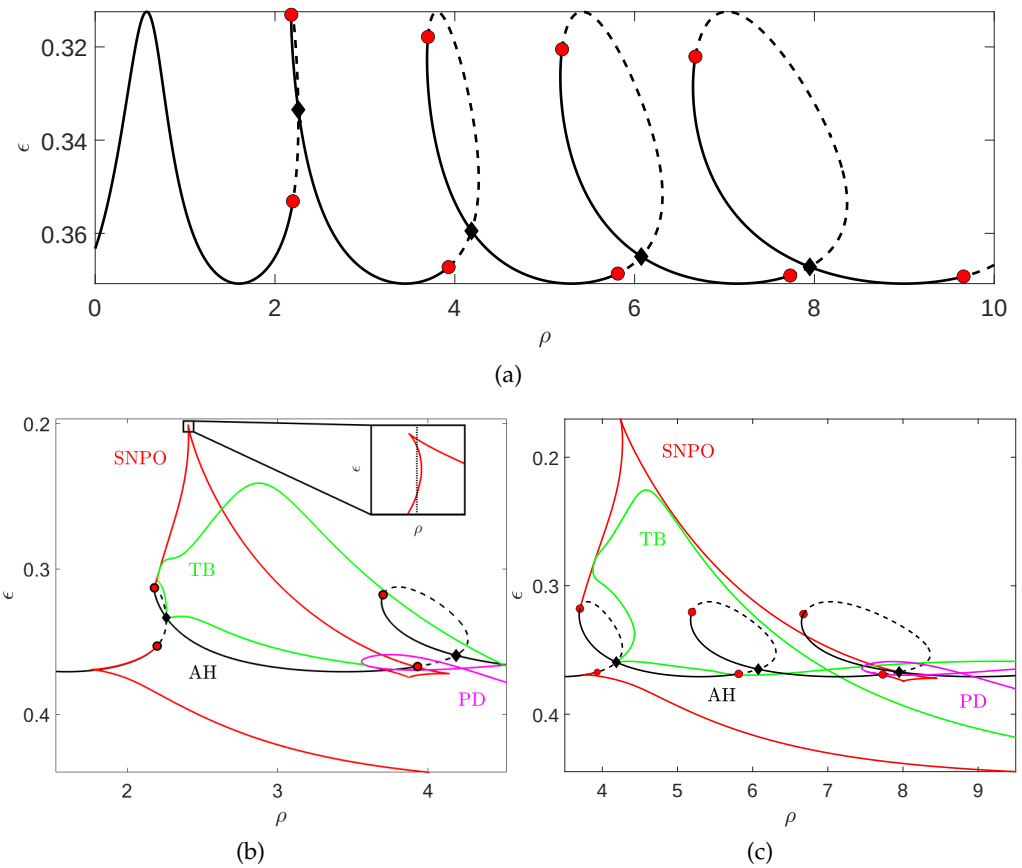

Figure 1. (a) Bifurcation diagram of the synchronised model in (3.1) depicting the onset of oscillatory solutions via Andronov-Hopf bifurcations (AH, black line). Solid lines denote supercritical Hopfs and dashed lines subcritical Hopfs, whilst red circles and black diamonds denote Bautin and double Hopf bifurcations, respectively. (b) A zoom in on (a) showing curves emanating from the first loop for the following bifurcations: saddle node of periodic orbits (SNPO, red line); torus bifurcations (TB, green line) and period doubling (PD, magenta line). (c) The periodic-like structure observed in (a) results in qualitatively similar bifurcation structures emanating from each loop, as can be seen by comparing curves emanating from the second loop (shown in (c)) against those in (b).

The first point of note is that the two pictures are qualitatively very similar, with a pair of torus bifurcations emerging from the double Hopf bifurcations and SNPO bifurcations emerging from each of the Bautin bifurcation points. In both instances, the SNPO emanating from the first Bautin bifurcation (as measured along the AH curve from left to right) results in a region, bounded above by the AH curve and below by the lower SNPO curve, in which the stable steady state coexists with a stable periodic orbit. In the region bounded below by the AH curve and to the right of the second Bautin bifurcation we observe the coexistence of multiple periodic solutions, both stable and unstable. For simplicity, consider the central region in Figure 1(b). Within this region, the stable periodic orbit born through the supercritical AH bifurcation loses stability either through a torus bifurcation (TB, green line in Figure1(b)) or through a period-doubling bifurcation (PD, magenta line in Figure 1(b)).

An additional interesting feature of the structures (TB, SNPO and PD branches) observed emanating from the second loop (Figure 1(c)) is an apparent stretching of the branches, relative to those emanating from the first (Figure 1(b)). Note that this branch stretching phenomenon appears to be a natural consequence of the reported widening of the AH bifurcation loop structure for

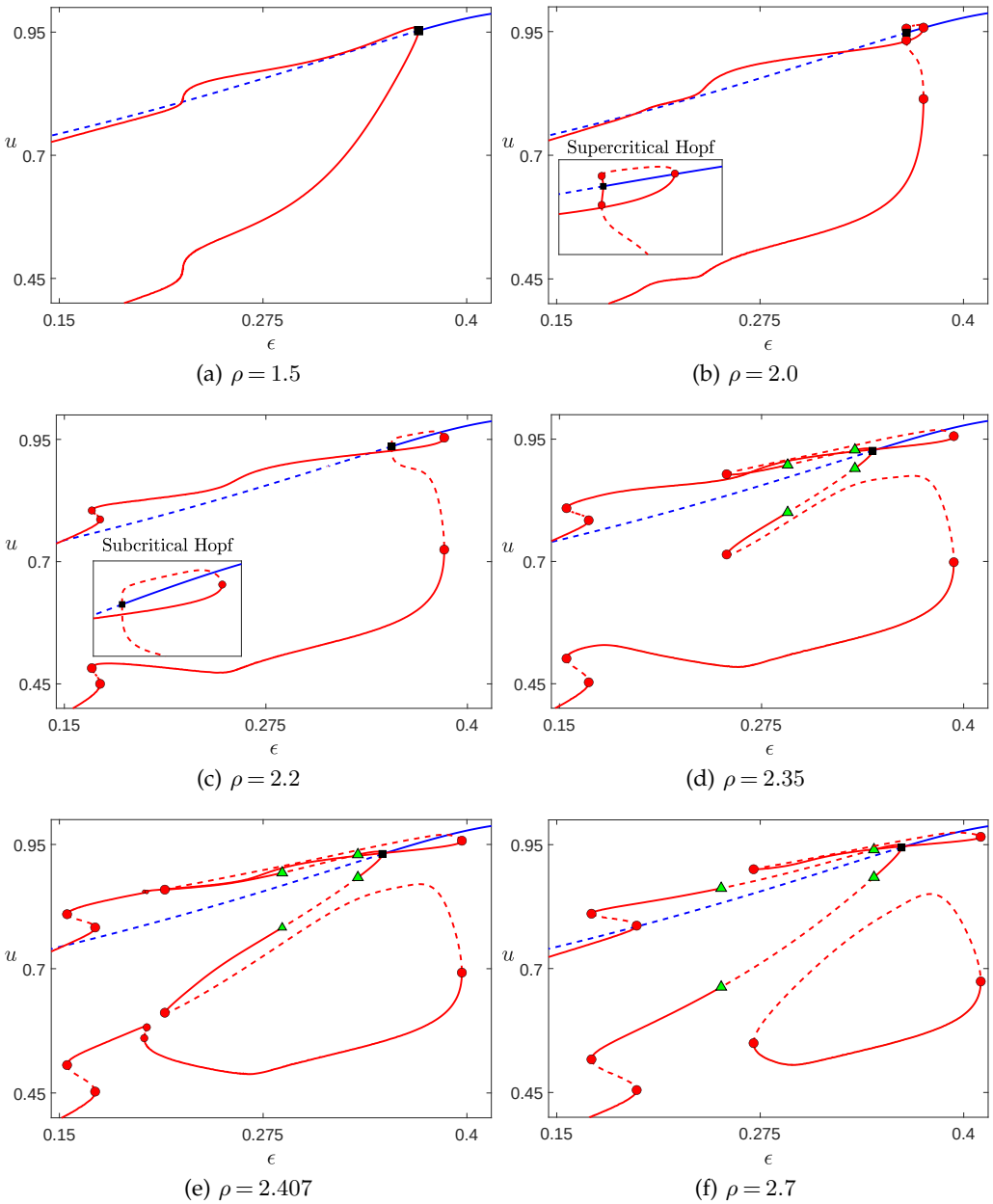

Figure 2. Vertical slices through Figure 1(b). Solid blue line, stable fixed points; dashed blue line, unstable fixed points; solid red lines, stable periodic orbits; dashed red line, unstable periodic orbits. The point labelled with a black square is an AH bifurcation, the points labelled with green triangles are torus bifurcations, and the points labelled with red circles are SNPO bifurcations. The parameter values are the same as in Figure 1. Note that only bifurcations showing the creation or destruction of stable objects are shown.

increasing delay time (see the discussion in [27,28] for further details), which leads to increasingly overlapped branches and a growing coexistence of both stable and unstable periodic orbits as the inter-nodal delay, ρ, increases. The intricate overlapping of branches, as depicted in Figure 1, results in a heightened sensitivity of the system, which in turn likely promotes metastability of

the network's dynamics as it transitions between different synchronous states under the influence of noisy inputs.

To better understand the solution structure of a typical looping branch, Figure 2 shows vertical slices through Figure 1 for several values of the inter-nodal delay parameter $\rho \in [1.5, 2.7]$. For $\rho = 1.5$ the system is monostable for all values of ϵ in that we either have a stable steady state or a stable periodic orbit (Figure 2(a)). Increasing the delay to $\rho = 2.0$, leads to a pair of saddle-node bifurcations of periodic orbits, which are created when the branch of periodic solutions reverses direction and creates a loop that winds about the AH point – see the zoomed-in inset in Figure 2(b). Increasing the delay to the value $\rho = 2.2$, so that it lies just beyond the first Bautin point, we detect a change of criticality for the AH point (see the zoomed-in inset in Figure 2(c)) and the destruction of the previously leftmost SNPO point, as well as the birth of a pair of new SNPO points towards the far left of the picture. For even larger delays we begin to observe more complex behaviours. Setting $\rho = 2.35$, so as to lie between the first double Hopf bifurcation and the upper SNPO branch cusp, gives the plot in Figure 2(d). Here, the AH bifurcation has reverted to being supercritical, since we have crossed the second Bautin point in Figure 1(b), but the resulting stable periodic orbit branch also loses stability in a narrow window of ϵ-values bounded by the two torus bifurcations. Additionally, we observe further folding of the periodic branch (via SNPO bifurcations), providing increased multistability. Approaching the cusp point from the left ($\rho = 2.407$, Figure 2(e)) we observe the birth of two additional SNPO points, which persist until the parameter ρ is further increased past the SNPO cusp ($\rho = 2.7$, Figure 2(f)), at which point two of the SNPO points collide, annihilating each other, whilst the third breaks off from the existing main branch of periodic orbits to form a new separate branch. In Figure 1(b), the inset provides a more detailed view of the SNPO cusp point structure. Specifically, it reveals the presence of four SNPO bifurcations within a small interval in ρ-parameter space, as previously described.

It is clear from the above analysis that the coexistence of multiple synchronous periodic solutions arises naturally in (2.1) as the inter-nodal delay parameter, ρ, is increased, and moreover, that the mechanisms underlying this multistability are manifold and include SNPO, torus and PD (not considered in the above analysis, which focussed on dynamics in the proximity of the first looping structure in Figure 1(a)) bifurcations.

Next we deploy parameter sweeps and Poincaré return maps to examine the aforementioned torus bifurcation scenario in more detail. It is well known that destabilisation of a periodic orbit through a TB can give rise to intricate system behaviour, including quasiperiodic and chaotic dynamics. Figures 3 and 4 illustrate characteristic stages of torus formation and breakdown for two different choices of the inter-nodal delay ρ. From the bifurcation diagram in Figure 3(a), for which $\rho = 2.9$, one can see that the stable periodic orbit, earlier emerging from the supercritical AH bifurcation, loses stability when ϵ is decreased through 0.351. This destabilisation gives rise to the emergence of a two-dimensional stable torus, the dynamics of which are initially ergodic or at least very weakly resonant. Note that the bifurcation diagram in Figure 3(a) was built using the Poincaré return map of consecutive minima (and maxima) of the excitable variable u, and shows a collation of ten randomly initialised parameter sweeps. This behaviour is further illustrated in Figures 3(b-d), which show the Poincaré return map of consecutive minima of the excitable variable $T : u_{\min}^{(n)} \longrightarrow u_{\min}^{(n+1)}$. Figure 3(b) shows a smooth invariant curve corresponding to an ergodic torus at $\epsilon = 0.337$. Decreasing ϵ we see that the torus becomes resonant with a stable periodic orbit on it (see Figures 3(c,d)). The degree of the resonance is determined by counting the number of periodic points of the stable periodic orbit, which is five in this instance, meaning that we have a $1:5$ resonance at $\epsilon = 0.333$. As the parameter ϵ is further reduced, we observe additional higher-order resonant zones which appear and disappear abruptly throughout the region of quasiperiodicity.

Figure 4 shows the results of a parameter sweep for $\rho = 2.7$. As evidenced in Figure 4(a), for this choice of the delay we appear to observe chaotic dynamics, the onset of which is preceded by the breakdown of the torus born from the TB at $\epsilon \approx 0.341$. To validate this observation we employed numerical integration to calculate the maximal Lyapunov exponent of Equation (3.1),

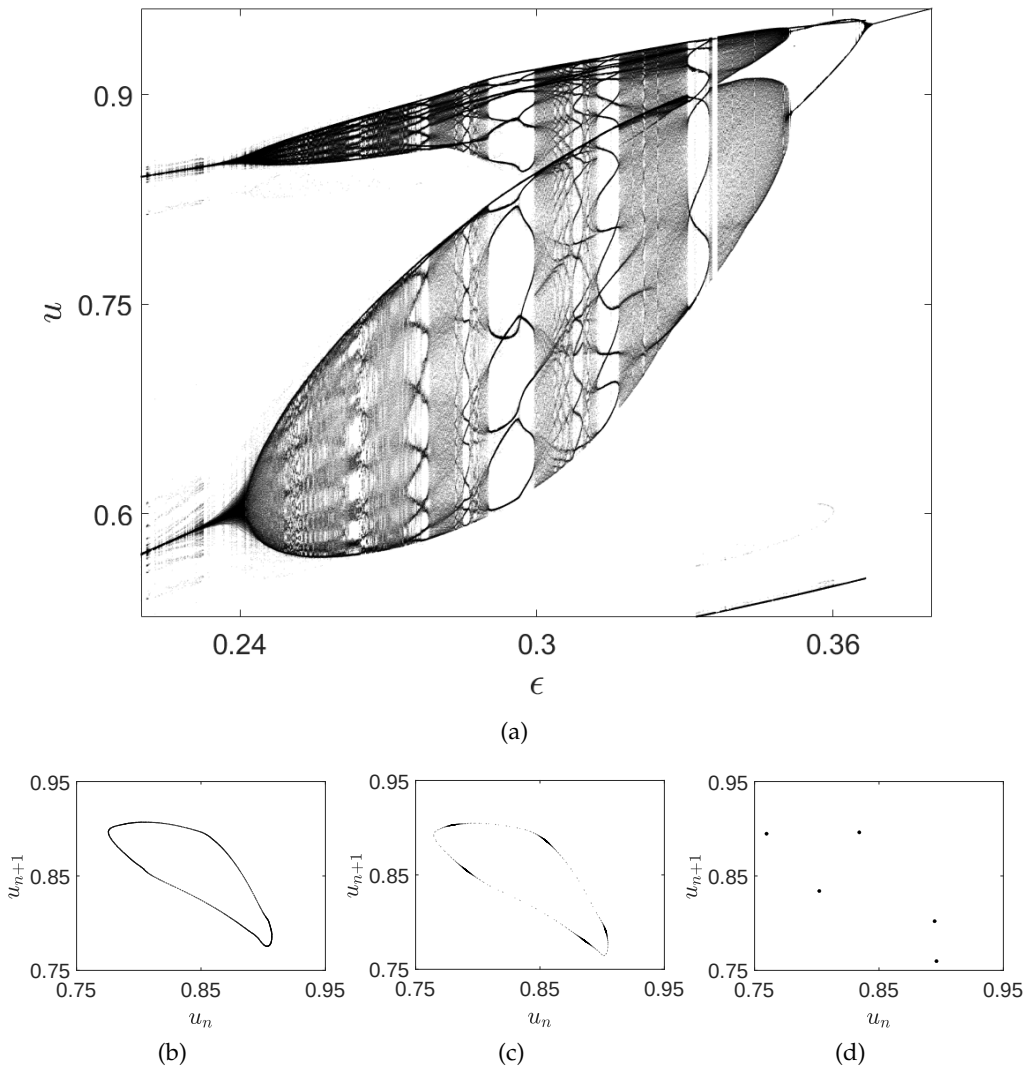

Figure 3. (a) Bifurcation diagram for $\rho = 2.9$ representing the ϵ-parameter sweep of the maximum and minimum values of u revealing the stability loss of the synchronised periodic solution through a torus bifurcation and the resulting quasiperiodic dynamics. (b)–(d) Poincaré return maps: $u_{\min}^{(n)} \to u_{\min}^{n+1}$ depicting the breakdown of the torus at $\rho = 2.9$. (b) Stable smooth invariant curve corresponding to an ergodic torus at $\epsilon = 0.337$. (c) For $\epsilon = 0.335$ we see that the torus approaches a resonant zone, in this case it is a 1:5 resonance. (d) A stable period-5 orbit at $\epsilon = 0.333$ after the torus breakdown.

while varying the inter-node delay, ρ and coupling strength, ϵ. This computation was carried out by simultaneously integrating the variational equation in parallel with the underlying system (as for ordinary differential equations [30]) for 100 randomly selected initial conditions. In particular, Figure 4(b) shows results indicating the emergence of delay-induced chaotic synchronisation in certain regions of parameter space. To further probe the highlighted region in Figure 4(b), in Figure 4(c) we plot the the Poincaré return map of consecutive minima of the excitable variable u for $(\rho, \epsilon) = (2.7, 0.27)$ (denoted by the white triangle in Figure 4(b)), which adds further weight to the suspected existence of a chaotic attractor for these parameter values. In particular, we find that the smooth invariant curve (see Figure 3(b), for such an example) born at the torus bifurcation

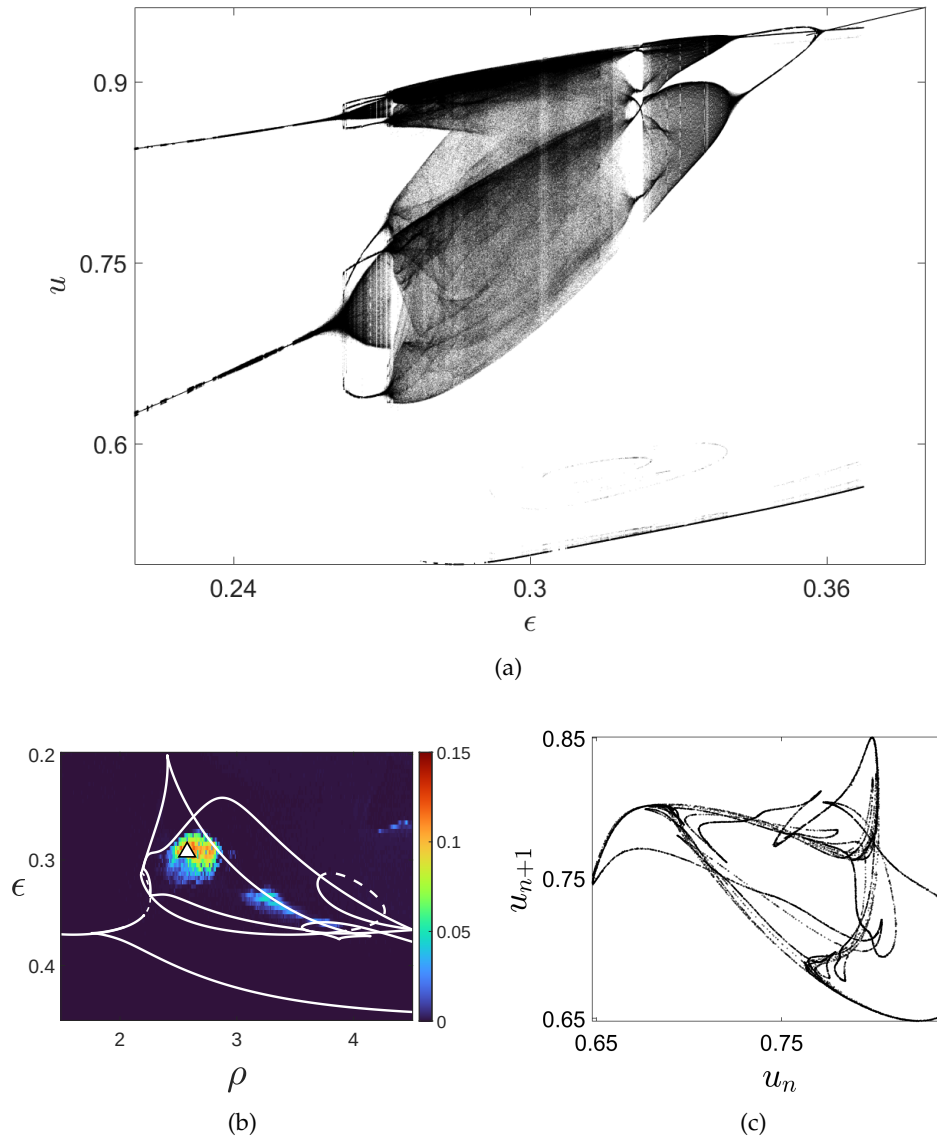

Figure 4. (a) Bifurcation diagram for $\rho = 2.7$ representing the ϵ-parameter sweep of the maximum and minimum values of u revealing the stability loss of the synchronised periodic solution through a torus bifurcation and the resulting chaotic dynamics. (b) Plot of the maximal Lyapunov exponent as a function of the delay parameter ρ and coupling strength ϵ for Equation (3.1). A positive exponent indicates chaotic behaviour. Values are obtained by averaging over 100 runs. We have also superimposed the bifurcation branches from Figure 1(b). (c) Poincaré return map $u_{\min}^{(n)} \to u_{\min}^{n+1}$ for consecutive $u_{\min}$ values provides evidence of a strange attractor at $(\rho, \epsilon) = (2.7, 0.27)$, which results from the breakdown of the torus.

becomes non-smooth (experiments not shown) for values of $\epsilon \approx 0.325$ and that this leads to a torus breakdown, followed by the emergence of more complex, chaotic dynamics as ϵ is further decreased – see, for example, the paper by Ju *et al.* [31] and references therein for a detailed description of the torus breakdown route to chaos. Note that this plot is typical for parameter values chosen from the 'chaotic regime' highlighted in Figure 4(b).

4. Ring of n bidirectionally coupled Wilson-Cowan masses

Thus far, our analysis has been restricted to the dynamics of the system (2.1) for initial conditions located on the synchronization manifold. In this section, we aim to broaden our understanding of the system by examining how these solutions generalise to arbitrary initial conditions, specifically in the context of a ring network architecture.

(a) Stability of the homogeneous steady state

Here, we consider a ring of n bidirectionally coupled, identical Wilson-Cowan masses. For this choice of architecture, the stability of the network steady state is governed by the equation

$$\det\left[I_n \otimes \left(\lambda I_2 - A - Be^{-\lambda\tau}\right) - \left(K + K^{n-1}\right) \otimes \left(C_\epsilon e^{-\lambda\rho}\right)\right] = 0,$$

where A, B are as in (3.4),

$$C_\epsilon = \begin{pmatrix} \frac{1}{2}\epsilon\beta u^*(1-u^*) & 0 \\ 0 & 0 \end{pmatrix},$$

and

$$K = \begin{pmatrix} 0 & 1 & 0 & \cdots & 0 \\ 0 & 0 & \ddots & \ddots & \vdots \\ \vdots & \vdots & \ddots & \ddots & 0 \\ 0 & 0 & \cdots & 0 & 1 \\ 1 & 0 & \cdots & 0 & 0 \end{pmatrix}$$

is the basic circulant permutation matrix [32].

Due to the block circulant structure of the above matrix, we can employ a discrete Fourier transform to diagonalise it [33], leading to the following factorized form of the characteristic equation:

$$\prod_{k=1}^{n} \det\left[\lambda I_2 - A - Be^{-\lambda\tau} - \left(e^{i\phi_k} + e^{i(n-1)\phi_k}\right) C_\epsilon e^{-\lambda\rho}\right] = 0,$$

where $\phi_k = 2\pi k/n, k = 1, \ldots, n$. Crucially, this equation can be solved numerically to determine the stability properties of the steady state solution of (2.1) as a function of the parameters ρ and ϵ, and hence reveal key bifurcation structures driving the observed dynamics of the full system.

The remainder of this section is devoted to a numerical exploration of the solution structure of a ring network architecture in the case of $n = 6$ masses.

(b) Bifurcation structure for a ring of 6 neural masses

Figure 5 shows curves of AH bifurcations of fixed points in the (ρ, ϵ) parameter plane for the full system in (2.1) with an undirected ring architecture on six nodes. In addition to the synchronous AH branch observed in Figure 1(a), which we denote here by a dash-dotted line, we find three further AH branches (black lines). As with our previous analysis, the stable steady state, which exists independent of ρ for sufficiently large coupling, destabilises via a supercritical AH bifurcation as the coupling parameter ϵ is decreased; however, in the networked case this typically leads to one of two distinct behaviours: either anti-phase synchronous solutions or completely synchronised solutions – see Figure 6 for an illustration of these different solution types. Note that the anti-phase synchrony we observe is a type of remote synchrony, previously detected in both toy network structures [34,35] and empirical brain networks [36], since nearest neighbours are out of phase. Crucially, the solution type depends upon how the fixed point destabilises (as ϵ is decreased); if stability is lost as we pass through the synchronous AH branch (indicated by the dash-dotted line in Figure 5) then the resulting solutions are synchronous, *i.e.* the synchronisation manifold $\mathcal{M}$ is stable, at least in the proximity of the first AH crossing. Otherwise, we observe

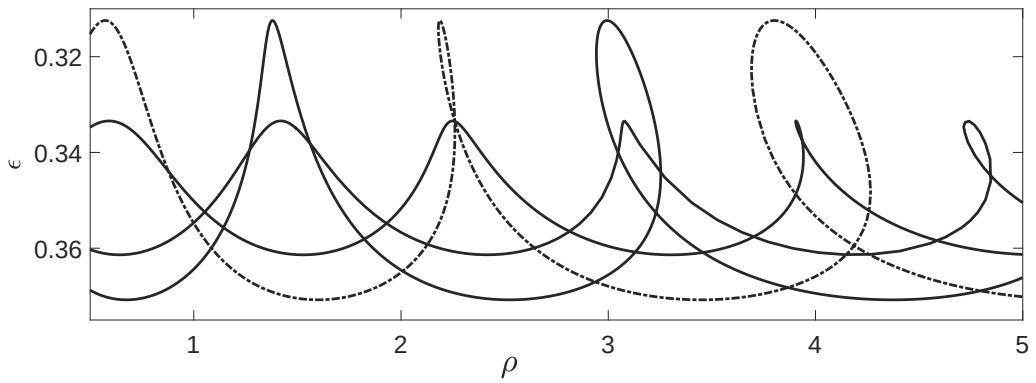

Figure 5. Bifurcation diagram of the full model in (2.1) for a ring network architecture with $n = 6$ nodes depicting the onset of oscillatory solutions via Andronov-Hopf bifurcations (black lines). The dash-dotted line marks the branch corresponding to synchronous solutions as shown in Figure 1(a).

anti-phase synchrony, again, local to the first AH branch. Due to the periodic-like crossings of the synchronous AH branch and the 'asynchronous' AH branch, this results in alternating regions of synchronous and anti-phase synchronous behaviour for increasing values of the delay ρ, at least away from any branch crossings, where we expect more complicated behaviour.

As noted above, at branch crossings, which are indicative of higher-dimensional bifurcations, we expect to observe more exotic dynamics such as the quasiperiodic and chaotic dynamics previously reported for the self-coupled system (3.1). To reveal regions of parameter space where complex dynamics exist, we computed the maximal Lyapunov exponent as a function of the control parameters (ρ, ϵ) for 100 randomly assigned initial conditions, following the methodology outlined in §3. Our results are shown in Figure 7, which additionally shows the superimposed AH curves of Figure 5 (white dashed and dash-dotted lines) and torus bifurcations of both anti-phase (dotted white line) and synchronous (solid white line) periodic solutions. It should be noted that a full bifurcation analysis of the networked system is not computationally feasible, given the additional complexities involved. As such, our focus in this section is to identify criticality boundaries that appear to influence the stability of the synchronization manifold.

For relatively weak coupling ($\epsilon < 0.2$) we observe intermittent bands of anti-phase and synchronous dynamics, which are delineated by weakly chaotic regions. In Figure 7, we highlight by a white circle and a white triangle respectively, the parameter values used to simulate the anti-phase and synchronous solutions displayed in Figure 6. Importantly, this banded structure repeats for larger values of the inter-nodal delay ρ (experiments not shown). As evidenced by the torus bifurcation branches (solid and dotted lines), for weak coupling transverse instabilities of the synchronisation manifold arise via the destabilisation of a periodic (or quasiperiodic) orbit leading us to conclude that the route to chaos here is via a torus breakdown, as previously described. For values of $\epsilon \approx 0.2$, we observe regions of parameter space for which intricate TB branch crossings occur, which results in increasingly complex dynamics, as indicated by an elevated maximal Lyapunov exponent. In particular, we observe the onset of multistable irregular dynamics, as evidenced in Figure 8, which displays four different solutions obtained by simulating (2.1) for the same fixed parameter values $(\rho, \epsilon) = (1.025, 0.205)$ (highlighted by a white square in Figure 7) and four randomly chosen initial conditions. These oscillatory solutions include examples of synchrony, phase locking and chaos across a range of frequencies.

As ϵ is further increased so as to approach the AH branches, the dynamics become increasingly sensitive; in particular, the stability of the synchronisation manifold can switch on and off rather abruptly as we traverse through this region of parameter space, due to the increase in the occurrence of branch crossings and the number of codimension two bifurcations. For example,

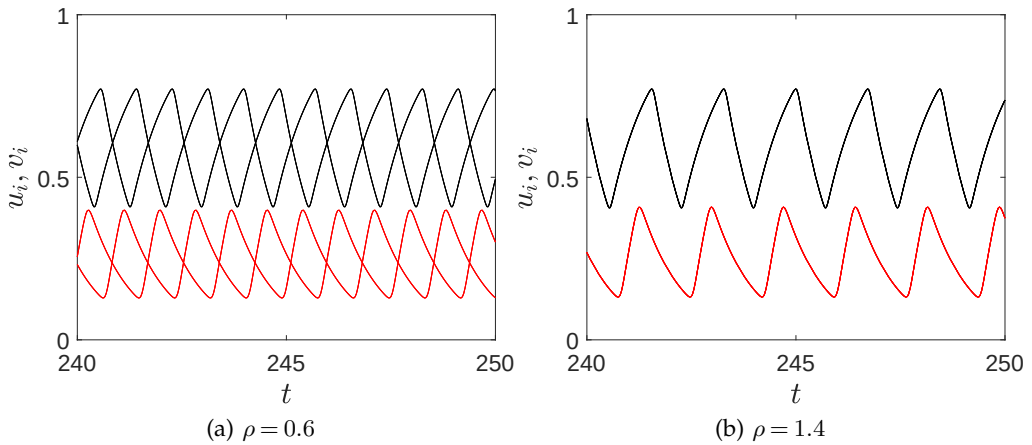

Figure 6. Profile comparisons of (a) anti-phase synchronous and (b) totally synchronised solutions of (2.1) with a bidirectional ring architecture on 6 nodes and $\epsilon = 0.1$. Black lines denote excitable variables u_i and red lines inhibitory variables v_i.

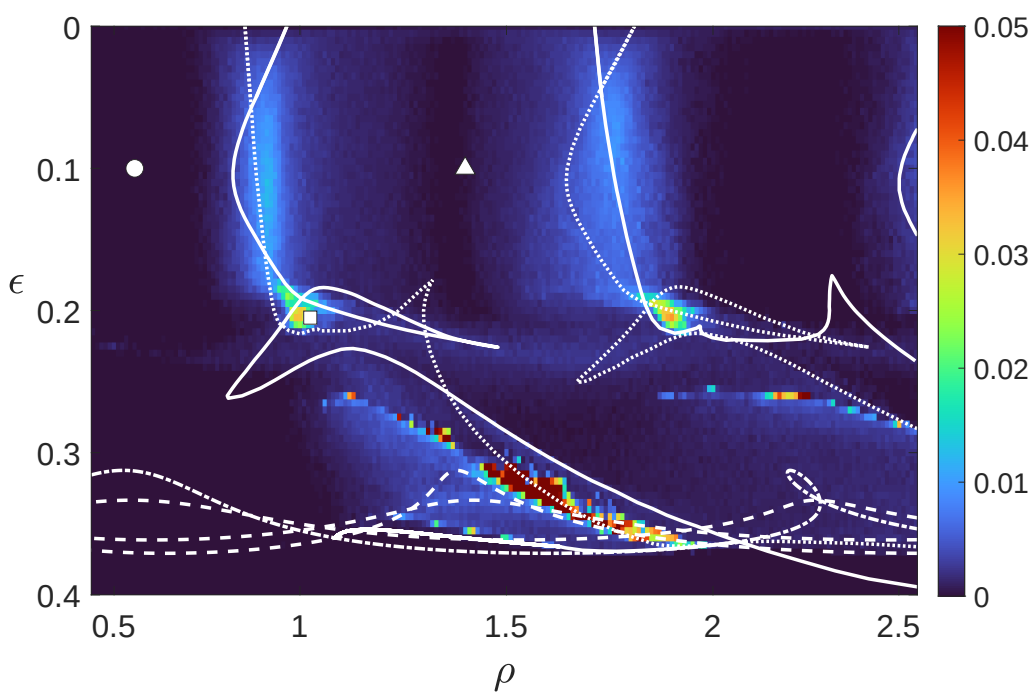

Figure 7. Plot of the maximal Lyapunov exponent of (2.1) as a function of of the delay parameter ρ and coupling strength ϵ. Results are averaged over 100 random initial conditions. Solid and dotted white lines denote a loss of stability via torus bifurcations for completely synchronised and anti-phase synchronised solutions, respectively. We have also superimposed the AH branches from Figure 5.

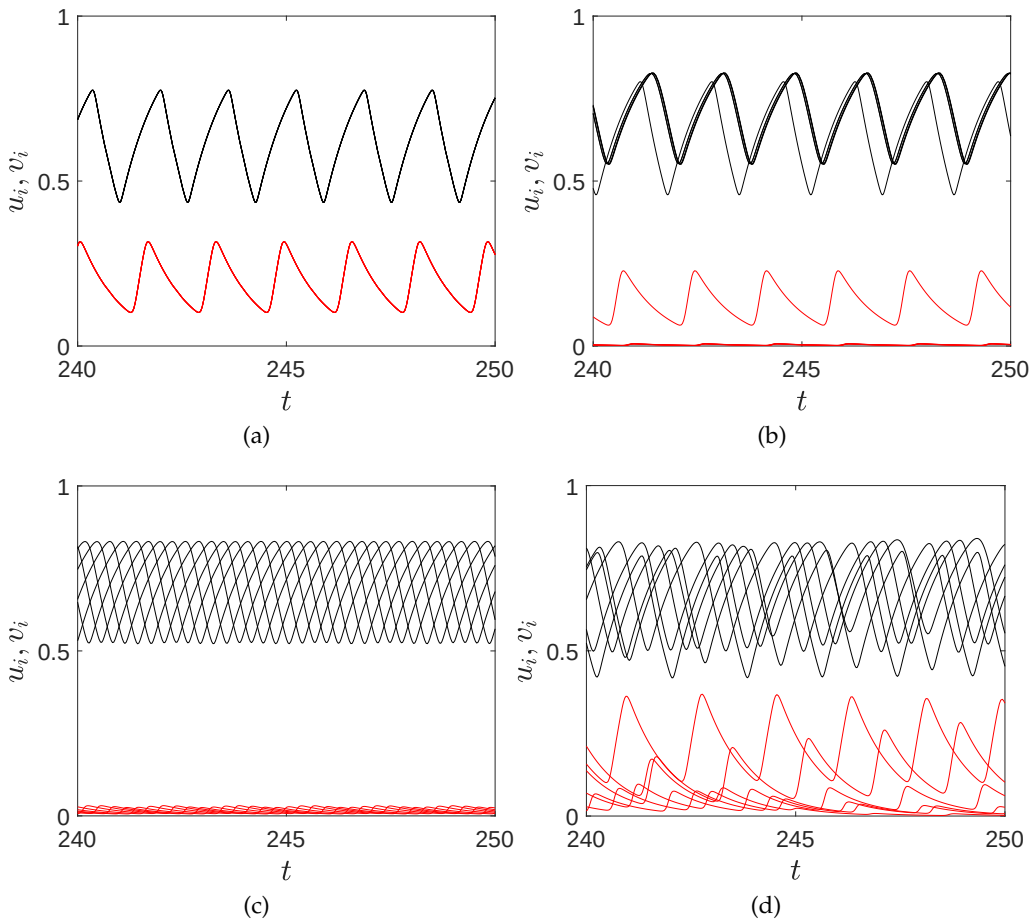

Figure 8. Figures (a)-(d) display exemplar solutions of (2.1) for four different initial conditions with the same parameter values $(\rho, \epsilon) = (1.025, 0.205)$, which we highlight with a white square in Figure 7. This type of multistability is typical for parameter values chosen close to branch intersections/higher-order bifurcations.

in Figure 7, we used numerical continuation to draw the TB branch connecting the double Hopfs that arise from the first two intersections of the synchronous and 'asynchronous' AH branches. Crucially, as we vary ϵ to cross this line, the synchronous solution born from the supercritical AH bifurcation destabilises due to the emergence of transverse instabilities in the synchronisation manifold. It is important to note that Figure 7 provides only a partial view of the intricate dynamics in this area, since several branches (including TB, SNPO and PD) that are known to generically emerge from the present codimension two bifurcations are excluded due to computational limitations. However, our numerical experiments indicate that the heightened parameter sensitivity within this multi-critical region of parameter space leads to complicated basin boundary structures that result in multistable dynamics, including anti-phase and complete synchrony over a range of frequencies and wave forms, as well as chaos.

We have focussed on the case $n = 6$ due to computational limitations; however, simulations on larger ring network structures (experiments not shown) suggest a qualitatively similar picture independent of n. For weak coupling we observe periodic switching between anti-phase and complete synchrony as observed in Figure 7 for $n = 6$, with solutions again separated by weakly chaotic regions. For larger networks, a key difference is the addition of a new AH branch for each pair of nodes added to the network, which leads to further branch crossings and increased

parameter sensitivity close to the AH branches as n is increased. Importantly, these additional AH branches are confined to the same region of parameter space as those displayed in Figure 5. It is also noteworthy that for n odd the anti-phase solution consists of $n-1$ nodes exhibiting anti-phase dynamics, while the remaining node oscillates independently, which is a kind of trivial chimera state [37].

5. Conclusion

In this paper, we have used numerical simulations (in Matlab) and computational bifurcation analysis (in DDE-BIFTOOL [26]) to investigate a bidirectional ring of Wilson-Cowan (WC) masses containing both intra- and inter-nodal delays. Unlike classical synchronisation studies, which typically consider diffusive coupling (see, for example, [24] and references therein), synchronous solutions of the system of WC nodes in (2.1) do not coincide with the uncoupled system, but rather with the self-coupled system in (3.1), as described by Campbell *et al.* [21,23] for a modified WC network model. Crucially, this means that the coupling strength ϵ can potentially modulate the synchronous dynamics of (2.1) in a nontrivial manner. By studying the self-coupled system, we find that the homogeneous steady state, which is present regardless of the inter-nodal delay for sufficiently large coupling, becomes destabilised through either a sub- or super-critical Andronov-Hopf (AH) bifurcation, depending on the magnitude of the inter-nodal delay. As is typical in systems with time delays [27], the AH branch for the self-coupled system exhibits a looping structure that introduces branch crossings and higher-dimensional bifurcations, which results in the emergence of multistable regions of parameter space in the proximity of the AH branch, including the coexistence of periodic orbits as well as more irregular, chaotic-like dynamics. By utilising Poincaré return maps, we identified the phenomenological scenario of torus breakdown, as previously proposed by Shilnikov [38], as the plausible pathway towards chaos in the self-coupled system.

Our investigations additionally emphasise the joint influence of network topology and time delay on the stability characteristics of synchronized solutions in a delayed neural mass system, such as the WC system examined in this study. For relatively weak of coupling, we observe a partitioning of the (ρ, ϵ) parameter space into a repetitive pattern of vertical stripes that exhibit synchronous or anti-phase synchronous behavior in an alternating manner. The boundaries of these regions are defined by areas of weak chaos, which emerge from transverse instabilities in the synchronisation manifold due to torus breakdown. Similar to the self-coupled node, augmenting the coupling strength leads to a progressively intricate dynamical landscape with more branch crossings, ultimately triggering the emergence of complex and multistable dynamics. Moreover, the numerical simulations conducted in this study suggest that the dynamics of the ring network retain their fundamental characteristics as the network size increases, although the parameter sensitivity near the AH branch and its associated structures tends to increase due to the presence of additional symmetries.

Future investigations shall focus on applications of the techniques deployed in this work to empirical brain networks derived from advanced MRI methodologies. Importantly, careful calibration of model parameters is necessary to accurately reproduce brain rhythms in this more realistic setting. In the current work, we chose parameters that were comparable to those used in [19], which allowed us to directly compare our results. However, further modifications are likely required to better represent the biology. For example, the constant time scaling between excitatory and inhibitory neurons used here may not be optimal from a physiological perspective. Nonetheless, the improved understanding of how dynamic network instabilities arise in simplified systems acquired from this study provides a solid foundation for the future analysis of the dynamic behaviour of these more complicated networked systems. Note that a recent study by Clusella *et al.* [39] discovered outcomes comparable to those demonstrated in this work for large-scale brain models without delay. In particular, the authors in [39] proposed that transverse instabilities in the synchronization manifold provide a possible mechanism underlying experimentally observed spatiotemporal neural activity. Given the results presented here, it

would be fascinating to investigate how the presence of delays affects dynamic brain network models. As seen in this work, the presence of high-codimension points (such as the observed double Hopf and Bautin bifurcations), where the system can explore parameter space whilst maintaining criticality [40,41], naturally leads to heightened parameter sensitivity resulting in metastable behaviour (in the presence of noisy system inputs) as the system transitions between synchronous and desynchronous states. Given the important role that such state-switching is believed to play in the brain's ability to dynamically adjust to changing environmental demands [42], further studies are necessary to determine the precise impact of high codimension bifurcations on shaping the dynamic landscape of brain network models [43]. Finally, owing to the fact that brain networks are intrinsically directed [44], it would be of great interest to extend the results of this study to directed networks. A handful of recent studies [45–47] have emphasised the role of network directionality on brain network dynamics. Thus, investigations into whether novel directed topology-driven instabilities of the synchronisation manifold exist is a crucial next step in understanding the spatiotemporal dynamics of these systems.

References

1. Tonnelier A, Meignen S, Bosch H, Demongeot J. 1999 Synchronization and desynchronization of neural oscillators. *Neural Networks* **12**, 1213–1228.
2. Uhlhaas P, Pipa G, Lima B, Melloni L, Neuenschwander S, Nikolić D, Singer W. 2009 Neural synchrony in cortical networks: history, concept and current status. *Frontiers in Integrative Neuroscience* p. 17.
3. Petkoski S, Spiegler A, Proix T, Aram P, Temprado JJ, Jirsa VK. 2016 Heterogeneity of time delays determines synchronization of coupled oscillators. *Physical Review E* **94**, 012209.
4. Choi H, Mihalas S. 2019 Synchronization dependent on spatial structures of a mesoscopic whole-brain network. *PLoS Computational Biology* **15**, e1006978.
5. Davis ZW, Benigno GB, Fletterman C, Desbordes T, Steward C, Sejnowski TJ, H. Reynolds J, Muller L. 2021 Spontaneous traveling waves naturally emerge from horizontal fiber time delays and travel through locally asynchronous-irregular states. *Nature Communications* **12**, 6057.
6. Sethia GC, Sen A, Atay FM. 2008 Clustered chimera states in delay-coupled oscillator systems. *Physical Review Letters* **100**, 144102.
7. Zakharova A, Loos S, Siebert J, Gjurchinovski A, Schöll E. 2015 Chimera patterns: influence of time delay and noise. *IFAC-PapersOnLine* **48**, 7–12.
8. Deco G, Jirsa V, McIntosh AR, Sporns O, Kötter R. 2009 Key role of coupling, delay, and noise in resting brain fluctuations. *Proceedings of the National Academy of Sciences* **106**, 10302–10307.
9. Ryu H, Campbell SA. 2020 Stability, bifurcation and phase-locking of time-delayed excitatory-inhibitory neural networks. *Mathematical Biosciences and Engineering* **17**, 7931–7957.
10. Campbell SA. 2007 Time delays in neural systems. *Handbook of Brain Connectivity* pp. 65–90.
11. David O, Friston KJ. 2003 A neural mass model for MEG/EEG: coupling and neuronal dynamics. *NeuroImage* **20**, 1743–1755.
12. Wilson HR, Cowan JD. 1972 Excitatory and Inhibitory Interactions in Localized Populations of Model Neurons. *Biophysical Journal* **12**, 1 – 24.
13. Carlu M, Chehab O, Dalla Porta L, Depannemaecker D, Héricé C, Jedynak M, Ersöz EK, Muratore P, Souihel S, Capone C et al.. 2020 50 Years of Modeling Neural Activity: Celebrating Jack Cowan's Career: A mean-field approach to the dynamics of networks of complex neurons, from nonlinear Integrate-and-Fire to Hodgkin–Huxley models. *Journal of Neurophysiology* **123**, 1042.
14. Campbell S, Wang D. 1996 Synchronization and desynchronization in a network of locally coupled Wilson-Cowan oscillators. *IEEE Transactions on Neural Networks* **7**, 541–554.
15. Hlinka J, Coombes S. 2012 Using computational models to relate structural and functional brain connectivity. *European Journal of Neuroscience* **36**, 2137–2145.
16. Rădulescu A, Verduzco-Flores S. 2015 Nonlinear network dynamics under perturbations of the underlying graph. *Chaos: An Interdisciplinary Journal of Nonlinear Science* **25**, 013116.
17. Muldoon SF, Pasqualetti F, Gu S, Cieslak M, Grafton ST, Vettel JM, Bassett DS. 2016 Stimulation-based control of dynamic brain networks. *PLoS Computational Biology* **12**,

e1005076.
18. Crofts JJ, Forrester M, Coombes S, O'Dea RD. 2022 Structure-function clustering in weighted brain networks. *Scientific Reports* **12**, 16793.
19. Coombes S, Laing C. 2009 Delays in activity-based neural networks. *Philosophical Transactions of the Royal Society A: Mathematical, Physical and Engineering Sciences* **367**, 1117–1129.
20. Conti F, Van Gorder RA. 2019 The role of network structure and time delay in a metapopulation Wilson–Cowan model. *Journal of Theoretical Biology* **477**, 1–13.
21. Nicola W, Hellyer PJ, Campbell SA, Clopath C. 2018 Chaos in homeostatically regulated neural systems. *Chaos: An Interdisciplinary Journal of Nonlinear Science* **28**, 083104.
22. Nicola W, Campbell SA. 2021 Normalized connectomes show increased synchronizability with age through their second largest eigenvalue. *SIAM Journal on Applied Dynamical Systems* **20**, 1158–1176.
23. Al-Darabsah I, Chen L, Nicola W, Campbell SA. 2021 The impact of small time delays on the onset of oscillations and synchrony in brain networks. *Frontiers in Systems Neuroscience* **15**, 688517.
24. Arenas A, Díaz-Guilera A, Kurths J, Moreno Y, Zhou C. 2008 Synchronization in complex networks. *Physics Reports* **469**, 93–153.
25. Pinder I, Crofts JJ. 2021 Oscillations and Synchrony in a Network of Delayed Neural Masses. *Rhythmic Oscillations in Proteins to Human Cognition* pp. 187–211.
26. Engelborghs K, Luzyanina T, Samaey G et al.. 2000 DDE-BIFTOOL: a Matlab package for bifurcation analysis of delay differential equations. *TW Report* **305**.
27. Yanchuk S, Perlikowski P. 2009 Delay and periodicity. *Physical Review E* **79**, 046221.
28. Kantner M, Yanchuk S. 2013 Bifurcation analysis of delay-induced patterns in a ring of Hodgkin–Huxley neurons. *Philosophical Transactions of the Royal Society A: Mathematical, Physical and Engineering Sciences* **371**, 20120470.
29. Seydel R. 2009 *Practical bifurcation and stability analysis* vol. 5. Springer Science & Business Media.
30. Sprott JC, Sprott JC. 2003 *Chaos and time-series analysis* vol. 69. Oxford university press Oxford.
31. Ju H, Neiman AB, Shilnikov AL. 2018 Bottom-up approach to torus bifurcation in neuron models. *Chaos: An Interdisciplinary Journal of Nonlinear Science* **28**, 106317.
32. Horn RA, Johnson CR. 2012 *Matrix analysis*. Cambridge University Press.
33. Davis PJ. 1979 *Circulant matrices*. Wiley New York.
34. Bergner A, Frasca M, Sciuto G, Buscarino A, Ngamga EJ, Fortuna L, Kurths J. 2012 Remote synchronization in star networks. *Physical Review E* **85**, 026208.
35. Minati L. 2015 Remote synchronization of amplitudes across an experimental ring of non-linear oscillators. *Chaos: An Interdisciplinary Journal of Nonlinear Science* **25**, 123107.
36. Vlasov V, Bifone A. 2017 Hub-driven remote synchronization in brain networks. *Scientific Reports* **7**, 10403.
37. Majhi S, Bera BK, Ghosh D, Perc M. 2019 Chimera states in neuronal networks: A review. *Physics of Life Reviews* **28**, 100–121.
38. Shilnikov A, Shilnikov L, Turaev D. 2004 On some mathematical topics in classical synchronization: a tutorial. *International Journal of Bifurcation and Chaos* **14**, 2143–2160.
39. Clusella P, Deco G, Kringelbach ML, Ruffini G, Garcia-Ojalvo J. 2023 Complex spatiotemporal oscillations emerge from transverse instabilities in large-scale brain networks. *PLOS Computational Biology* **19**, e1010781.
40. Cocchi L, Gollo LL, Zalesky A, Breakspear M. 2017 Criticality in the brain: A synthesis of neurobiology, models and cognition. *Progress in Neurobiology* **158**, 132–152.
41. Zimmern V. 2020 Why brain criticality is clinically relevant: a scoping review. *Frontiers in Neural Circuits* **14**, 54.
42. Tognoli E, Kelso JS. 2014 The metastable brain. *Neuron* **81**, 35–48.
43. Gross T. 2021 Not one, but many critical states: a dynamical systems perspective. *Frontiers in Neural Circuits* **15**, 614268.
44. Kale P, Zalesky A, Gollo LL. 2018 Estimating the impact of structural directionality: How reliable are undirected connectomes?. *Network Neuroscience* **2**, 259–284.
45. Asllani M, Challenger JD, Pavone FS, Sacconi L, Fanelli D. 2014 The theory of pattern formation on directed networks. *Nature communications* **5**, 4517.
46. Padmore A, Nelson MR, Chuzhanova N, Crofts JJ. 2020 Modelling the impact of structural directionality on connectome-based models of neural activity. *Journal of Complex Networks* **8**, cnaa033.

47. Crofts JJ, Chuzhanova N, Padmore A, Nelson MR. 2022 Synchrony in directed connectomes. *Europhysics Letters* **139**, 42004.